


CO₂ outgassing during collisional orogeny is facilitated by the generation of immiscible fluids

Chiara Groppo ^{1,2} , Franco Rolfo ^{1,2} & Maria Luce Frezzotti ³

Orogenic degassing is emerging as a potentially relevant source of carbon dioxide (CO₂) from the continental crust. However, the processes of carbon mobilization are still poorly explored. Here, we use thermodynamic modeling to investigate the decarbonation of sediments metamorphosed under high geothermal gradients. Our modeling shows that immiscible CO₂-rich vapors and hydrosaline brines are generated at these conditions, with different properties and mobility through the crust. The CO₂-rich fluid fraction could rapidly rise toward the surface without interacting with the host rocks by carbo-fracturing the host rocks or through deep faults. The denser hydrosaline brines likely permeate the source rocks. When applied to the active Himalayan orogen, these observations reconcile measured CO₂ fluxes at the surface and positive conductivity anomalies associated with micro-seismicity at depth. Our modeling shows that the continental crust represents a relevant reservoir of CO₂ that can be efficiently degassed during hot collisions.

¹Department of Earth Sciences, University of Torino, via Valperga Caluso 35, 10125 Torino, Italy. ²CNR-IGG, via Valperga Caluso 35, 10125 Torino, Italy.
³Department of Earth and Environmental Sciences, University of Milano Bicocca, Piazza della Scienza 1, 20126 Milano, Italy. email: chiara.groppo@unito.it

Although the global Earth's natural CO₂ degassing is considered irrelevant compared to anthropogenic emissions, much effort is devoted to assessing our planet contribution to the global carbon cycle. Knowing the rate of the Earth's natural CO₂ emissions is, in fact, crucial for quantifying and predicting the influence of anthropogenic perturbations on climate processes¹. It is well known that metamorphism of crustal rocks in collisional orogens produces carbon-bearing fluids over geologic time scales, primarily through decarbonation reactions^{2–7}. However, the potential contribution of orogenic processes to the global Earth's carbon cycle is a long-standing open question^{5,8–12}. The efficiency of metamorphic CO₂ degassing in orogenic settings is primarily controlled by the ease at which the CO₂-bearing aqueous fluids produced at depth are transported upward without interacting with the host rocks. Fluid-rock interactions following prograde metamorphic devolatilization reactions can lead to carbon re-precipitation typically as carbonate^{13–21} or graphite^{22,23}, thus hampering significant CO₂ outgassing at the surface. The ability (or inability) of deep CO₂ to migrate upward and reach the Earth's surface opens up two possible scenarios. If retrograde metamorphism represents a sink for CO₂¹², collisional orogens' contribution to the global Earth's CO₂ degassing would be minimal. Conversely, if metamorphic CO₂-bearing fluids do not react with the host rocks, orogenic decarbonation would represent an important source of CO₂ at the global scale. Recent research⁷ balancing estimates of decarbonation rates from deeply exhumed rocks^{24–26} and CO₂ fluxes measured at the surface^{9,27,28}, support the second hypothesis. However, neither were the physical and chemical characteristics of the released metamorphic fluids studied in detail nor was the transport path of deep CO₂ fully elucidated.

Here, we study decarbonation reactions occurring in carbonate-bearing sediments along high geothermal gradients to define the physical and chemical nature of fluids that transport carbon in large hot orogens. We find that the productivity of CO₂-rich fluids is maximum for carbonate-bearing sediments originally containing low to moderate amounts of calcite (10–30 vol%) and metamorphosed at medium- to high-temperature (*T*) (i.e., *T* > 600 °C) and at medium pressure (*P*) (i.e., *P* > 8 kbar) conditions. We present petrological evidence that most dehydration and decarbonation reactions in these lithologies occur at *P*–*T* conditions in the two-phase field of the H₂O–CO₂–salt ternary fluid systems, generating immiscible CO₂-rich vapors and hydrosaline brines. Our results demonstrate a crucial role of fluid immiscibility in driving CO₂ transport from the deep crust, explaining how and why significant amounts of CO₂ could be effectively degassed at the surface from orogenic belts. This study reconciles geophysical and geochemical observations from active collisional orogens such as the Himalaya, where intense CO₂ degassing is currently measured at the surface. Results further highlight the role of hydrosaline brines as metasomatizing and/or granulitizing agents in the lower crust.

Results

Fluid production and evolution in large hot orogens. In large hot orogens (i.e., mountain belts characterized by high crustal temperatures and extreme crustal thickening^{29,30}), CO₂ sources are represented mainly by carbonate-bearing sediments ranging from calcareous pelites to marls and impure limestones, important constituents of thick sedimentary sequences deposited along passive margins³¹. During prograde metamorphism along medium to high *dT/dP* gradients, these lithologies are transformed into calcic metapelites, calc-silicate rocks, and silicate-bearing marbles and generally show an internally buffered behavior^{24,31–33}. Phase equilibria modeling of carbonate-bearing sediments obtained as “synthetic” mixtures of variable proportions of calcite (i.e., 10, 30, 50,

70 vol%, corresponding to initial bulk compositions Cal10, Cal30, Cal50, and Cal70; Table 1) with an average pelite³⁴ allows predicting the fluid evolution and compositions along a *dT/dP* geothermal gradient typical of large hot orogens (i.e., 750 °C GPa^{−1}, ca. 25 °C km^{−1} (see ref. 35)). The results of the modeling are illustrated in Figs. 1 and 2.

In carbonate-bearing metasediments, volatiles (H₂O and CO₂) are primarily hosted in phyllosilicates and carbonates; scapolite can represent an additional, often neglected, CO₂ reservoir^{24,25,31,36}. Prograde metamorphism generates C–O–H fluids dominated by H₂O and CO₂ components, the amounts of the other molecular species (CO, CH₄, and H₂) being negligible (i.e., <0.005 mol%) for all the investigated bulk compositions (Supplementary Data Files S1–S4). The aqueous component of the released C–O–H fluids is generated chiefly by the breakdown of chlorite, muscovite, biotite and/or epidote, and the CO₂ component by calcite and/or scapolite consumption. The interplay between formation and consumption of these phases controls the relative amounts of H₂O and CO₂ that can be released at increasing *P*–*T* conditions (i.e., if biotite forms during the muscovite breakdown, part of the H₂O is transferred from muscovite to biotite and, similarly, if scapolite formation coincides with calcite consumption, part of the CO₂ produced through calcite breakdown is fixed in scapolite). The results of the modeling show that, independently from the original amount of calcite in the sedimentary protolith, the production of C–O–H fluids in internally buffered carbonate-bearing metasediments mainly occurs in pulses (Figs. 1b, d and 2b, d), i.e., through nearly discontinuous reactions operating in narrow *P*–*T* intervals (see also refs. 24,25,31).

Two main events of CO₂ production are predicted at 575–605 °C (event I) and 630–670 °C (event II), respectively. For any of the modeled initial bulk compositions, event I corresponds to the muscovite-out reaction R1: Cal + Qz + Mu + Pl = Kfs + Scp + F, nearly coinciding with the total consumption of calcite for Cal10 bulk composition. Event II corresponds to the scapolite-out reaction R2a: Bt + Qz + Scp = Kfs + Cpx + Grt + Pl + F for Cal10 bulk composition; for Cal30, Cal50 and Cal70 bulk compositions, event II coincides with the biotite-out reaction

Table 1 Modeled bulk compositions (mol%) and approximate protolith's mineral compositions (vol%).

	Ague, 1991	Cal10	Cal30	Cal50	Cal70
SiO ₂	70.19	65.59	54.83	42.54	28.10
Al ₂ O ₃	11.69	10.92	9.13	7.08	4.68
TiO ₂	0.67	0.63	0.52	0.41	0.27
FeO	6.44	6.02	5.03	3.90	2.58
MnO	0.09	0.08	0.07	0.05	0.04
MgO	4.67	4.36	3.65	2.83	1.87
CaO	1.81	8.23	23.29	40.49	60.72
Na ₂ O	1.75	1.64	1.37	1.06	0.70
K ₂ O	2.70	2.52	2.11	1.64	1.08

	Av pelite	Calcareous pelite	Marl	Marl	Impure limestone
	Cal0	Cal10	Cal30	Cal50	Cal70
Kao	0	0	0	0	0
Ill	29	26	20	14	9
FeChl	11	10	8	6	3
MgChl	8	7	6	4	2
Qz	33	29	23	16	10
Cal	0	10	30	50	70
Ab	13	12	9	6	4
Kfs	0	0	0	0	0
An	6	6	4	3	2

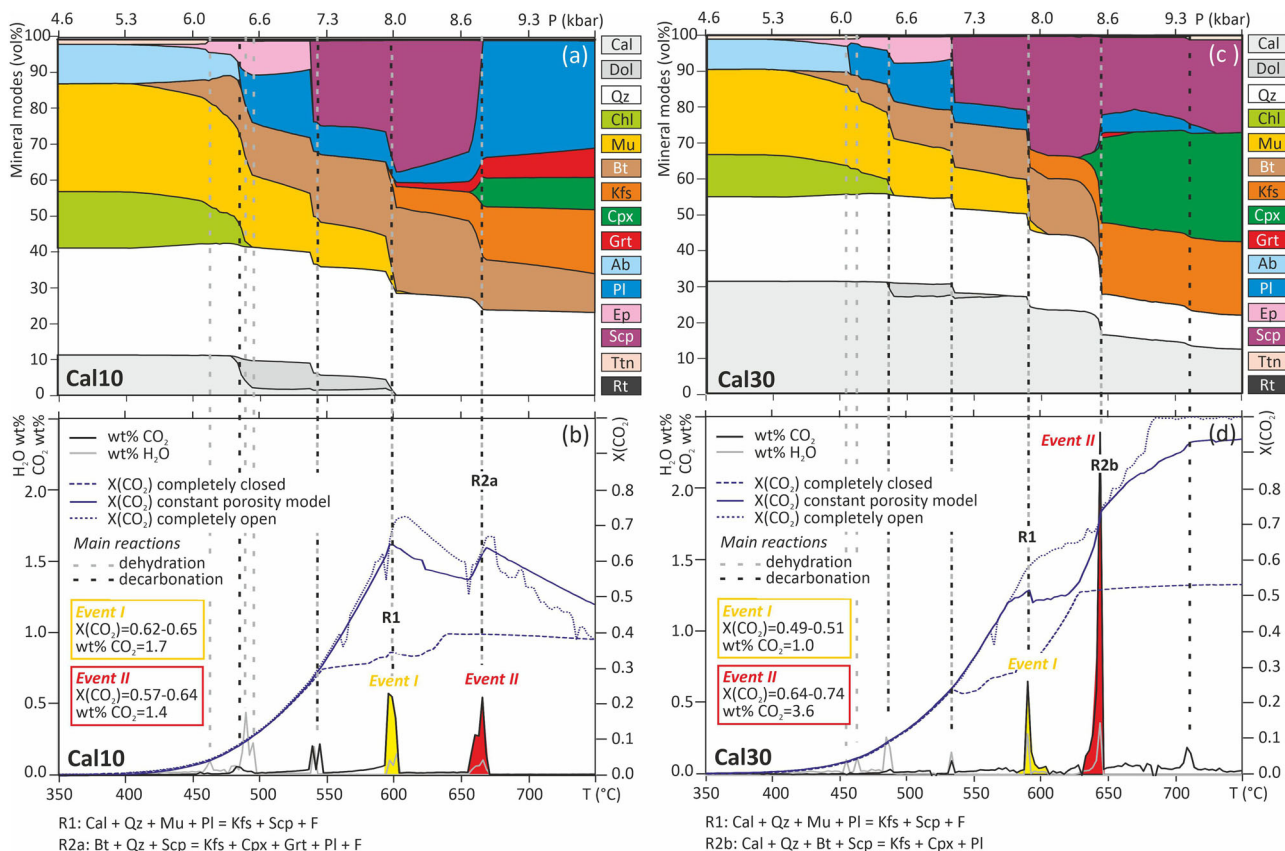


Fig. 1 Modal variations and wt% of CO₂ and H₂O released during prograde metamorphism of Cal10 and Cal30 bulk compositions. **a, c** Mode box changes in calculated mineral proportions (vol%, fluid excluded) during prograde metamorphism of sediments initially containing (a) 10 vol% of calcite (Cal10) and (c) 30 vol% of calcite (Cal30) along the modeled internally buffered *P/T*-*X*(CO₂) paths. **b, d** Loss (wt%) of CO₂ (black line) and H₂O (gray line) relative to the initial CO₂ and H₂O content in the solids, and *X*(CO₂) of the fluid (blue lines) released during prograde metamorphism of Cal10 (b) and Cal30 (d), along the same internal buffered *P/T*-*X*(CO₂) path as in (a) and (c). Events I (yellow) and II (red) refer to the main events of CO₂ production, as discussed in the text. Dashed lines highlight the main dehydration and decarbonation reactions, corresponding to abrupt consumption and/or complete disappearance of hydrous and CO₂-bearing minerals. Reactions corresponding to the event I (R1) and event II (R2a, R2b) are specified.

R2b: $\text{Cal} + \text{Bt} + \text{Qz} + \text{Scp} = \text{Kfs} + \text{Cpx} + \text{Pl} + \text{F}$ (Figs. 1 and 2). At each event, the fluid composition (*X*(CO₂) = molar fraction of CO₂) varies depending on the initial bulk composition (Figs. 1 and 2). The *X*(CO₂) generally increases at increasing temperatures (i.e., from event I to event II), except for Cal10 where the maximum *X*(CO₂) is reached at event I (Fig. 1b). The *X*(CO₂) of the fluids released at event II is generally higher than 0.5, with maximum values of *X*(CO₂) = 0.64–0.74 (Cal30; Fig. 1d), whereas it is more variable for fluids released at event I, ranging from *X*(CO₂) = 0.62–0.65 (Cal10; Fig. 1b) to *X*(CO₂) = 0.30–0.33 (Cal70; Fig. 2d). The amount of CO₂ (i.e., wt% loss of CO₂ relative to the initial CO₂ content in the solids) produced at each event increases up-temperature, except for Cal10, for which event I releases slightly more CO₂ than event II (Fig. 1b). The total CO₂ productivity increases from Cal10 (4.7 wt%) to Cal30 (7.0 wt%) and then decreases for Cal50 (3.7 wt%) and Cal70 (1.9 wt%). The same trend is observed when considering the CO₂ productivity related to event II only, maximum for Cal30 (3.6 wt%; Fig. 1d) and minimum for Cal70 (0.5 wt%; Fig. 2d).

Our results show that CO₂ is an essential component of C–O–H fluids released at relatively high temperatures (630–670 °C) and medium pressures (8.4–8.9 kbar or 25–30 km depth) during the formation of large hot orogens. The CO₂ productivity is maximum for the carbonate-bearing sediments originally containing low to moderate modal amounts of calcite (i.e., Cal10 and Cal30; Fig. 1) (see also refs. 24,25,31), whereas it is considerably lower in impure limestones (Cal70)³⁷. Also, the model predictions are in excellent

agreement with those discussed in recent papers focused on thermodynamic modeling of natural rock samples^{24,25,31,38} and with fluid inclusion studies providing direct measurements of the fluid composition in mixed pelitic–carbonatic metamorphic sequences from collisional orogens^{39–41}. As a step forward, determining the physical and chemical properties of the fluids generated at these *P*–*T* conditions would be essential for understanding their behavior and, ultimately, the connection between the deep metamorphic production of CO₂ in the crust and its release at the surface.

Fluid immiscibility in the H₂O–CO₂–salt systems. Traditionally, metamorphic fluids have been considered as binary CO₂–H₂O mixtures in most thermodynamic modeling studies^{42–45}. However, fluids derived from metasedimentary rocks originally deposited at continental passive margins such as those involved in large hot orogens are generally characterized by variable, relatively high salinity (i.e., from 5 to 50–60 wt% NaCl eq.) even at high metamorphic grades, reflecting the presence of highly saline pore water and/or evaporites in the initial sedimentary sequence^{37,46–49}. Thick layers of evaporites are well known to occur along present-day passive margins, where they control the formation and storage of oil and gas^{50,51}, but they are also common in ancient sedimentary sequences since the Proterozoic ages^{52,53}. Direct evidence for saline fluids in metamorphosed passive margin sequences is represented by rare halide minerals, fluid inclusions, and/or high Cl contents of

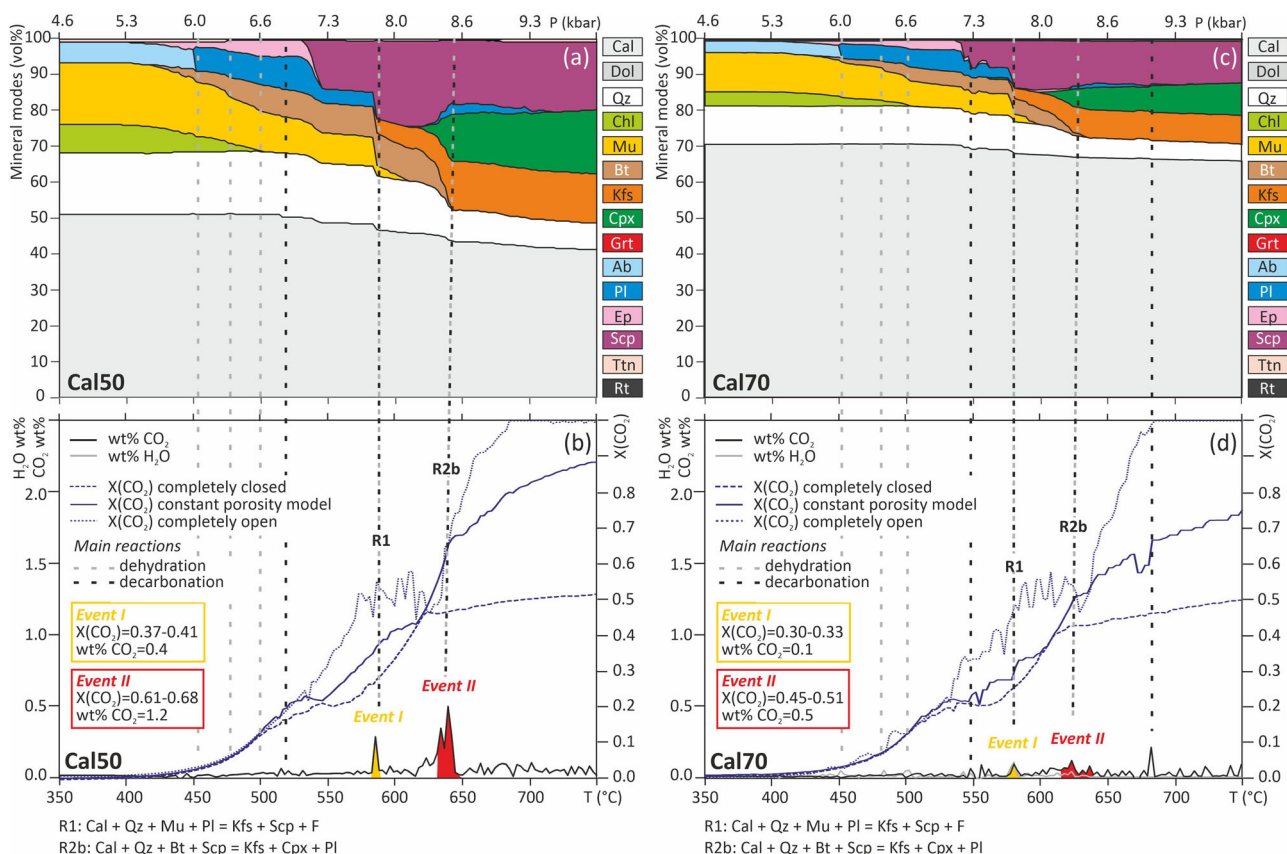


Fig. 2 Modal variations and wt% of CO₂ and H₂O released during prograde metamorphism of Cal50 and Cal70 bulk compositions. **a, c** Mode box changes in calculated mineral proportions (vol%, fluid excluded) during prograde metamorphism of sediments initially containing (a) 50 vol% of calcite (Cal50) and (c) 70 vol% of calcite (Cal70) along the modeled internally buffered *P/T-X(CO₂)* paths. **b, d** Loss (wt%) of CO₂ (black line) and H₂O (gray line) relative to the initial CO₂ and H₂O content in the solids, and *X(CO₂)* of the fluid (blue lines) released during prograde metamorphism of Cal50 (b) and Cal70 (d), along the same internal buffered *P/T-X(CO₂)* path as in (a) and (c). Events I (yellow) and II (red) refer to the main events of CO₂ production, as discussed in the text. Dashed lines highlight the main dehydration and decarbonation reactions, corresponding to abrupt consumption and/or complete disappearance of hydrous and CO₂-bearing minerals. Reactions corresponding to the event I (R1) and event II (R2b) are specified.

key high-grade metamorphic minerals^{54–57}. Evidence for salinity dilution at high temperatures due to progressive dehydration is feeble, suggesting that even advanced metamorphic dehydration cannot flush away the salinity inherited from the protoliths^{46,47,52}.

In this framework, salts components are particularly relevant because they strongly influence the topology of fluid phase equilibria, expanding the two-phase immiscibility fields^{37,46,47,58–61}. Fluid(s) produced by decarbonation reactions of calcite-bearing sedimentary protoliths can be reasonably described by the H₂O–CO₂–NaCl system^{40,57,62–64} and the H₂O–CO₂–CaCl₂ system^{41,65}. These ternary systems have been studied experimentally from 1 to 9 kbar and from 400 to 1000 °C^{64,66–70}, i.e., at *P–T* conditions compatible with those attained in large hot orogens. In order to describe phase relations of fluids produced during the main events of CO₂ production (i.e., event I: 575–605 °C, 7.6–8.0 kbar; event II: 630–670 °C, 8.3–9.0 kbar), we have interpolated the H₂O±CO₂–salts ternary diagrams obtained experimentally by ref.⁶⁹ at 800 °C, 9 kbar and 500 °C, 5 kbar. The phase diagrams resulting from these interpolations (Figs. 3 and 4) are valid at ca. 575 °C, 6 kbar (i.e., for event I) and at ca. 650 °C, 7 kbar (i.e., for event II).

In the H₂O–CO₂–NaCl system, the evolution of the fluids produced during the most CO₂-productive event II proceeds as a function of the initial bulk-rock composition and the initial salinity. Fluids generated during event II have an *X(CO₂)* systematically higher than 0.4 (Cal10: *X(CO₂)* = 0.57–0.64; Cal30: *X(CO₂)* = 0.64–0.74; Cal50: *X(CO₂)* = 0.61–0.68; Cal70:

X(CO₂) = 0.45–0.51; Figs. 1b, d and 2b, d). In the hypothesis of a bulk salinity of 10 wt% NaCl, these fluids plot in the miscibility gap (Fig. 3b, d, f and Supplementary Fig. S1b), either in the vapor + liquid (V + L) two-phase field (Cal10, Cal50, and Cal70), or in the vapor + salt (V + NaCl) two-phase field (Cal30). In the first case, once liberated, fluids would inevitably split into a CO₂-rich phase of a lesser density (i.e., vapor⁶²) (Cal10: CO₂ = 60–66 mol%; Cal50: CO₂ = 62–66 mol%; Cal70: CO₂ = 49–53 mol%; Table 2) and a highly saline aqueous phase (i.e., liquid⁶²) (Cal10: NaCl = 38–42 mol%; Cal50: NaCl = 40–42 mol%; Cal70: NaCl = 23–30 mol%; Table 2), with the CO₂-rich vapor being the dominant fluid type (i.e. >85 mol%; Fig. 3b, f and Supplementary Fig. S1b). For Cal10 and Cal50 bulk compositions, the segregation of low amounts of halite from the two immiscible fluids (i.e., three-phase field V + L + NaCl; Fig. 3b, f) is predicted for the highest *X(CO₂)* values of the produced fluid. In the second case, a single vapor-like CO₂-rich fluid (Cal30: CO₂ = 66–73 mol%; Table 2) would coexist with solid halite. The immiscible nature of the fluids produced at the *P–T* conditions of event II is further amplified for higher initial fluid salinity, resulting in a more enriched CO₂ vapor and a hydrosaline brine with higher salinity; the fraction of the brine increases with initial salinity.

A similar evolution is predicted for the fluid produced at event I in the H₂O–CO₂–NaCl system (Fig. 3a, c, e and Supplementary Fig. S1a). At *T* = 595–605 °C and *P* = 7–8.0 kbar, Cal10 bulk composition generates a fluid whose CO₂-rich composition

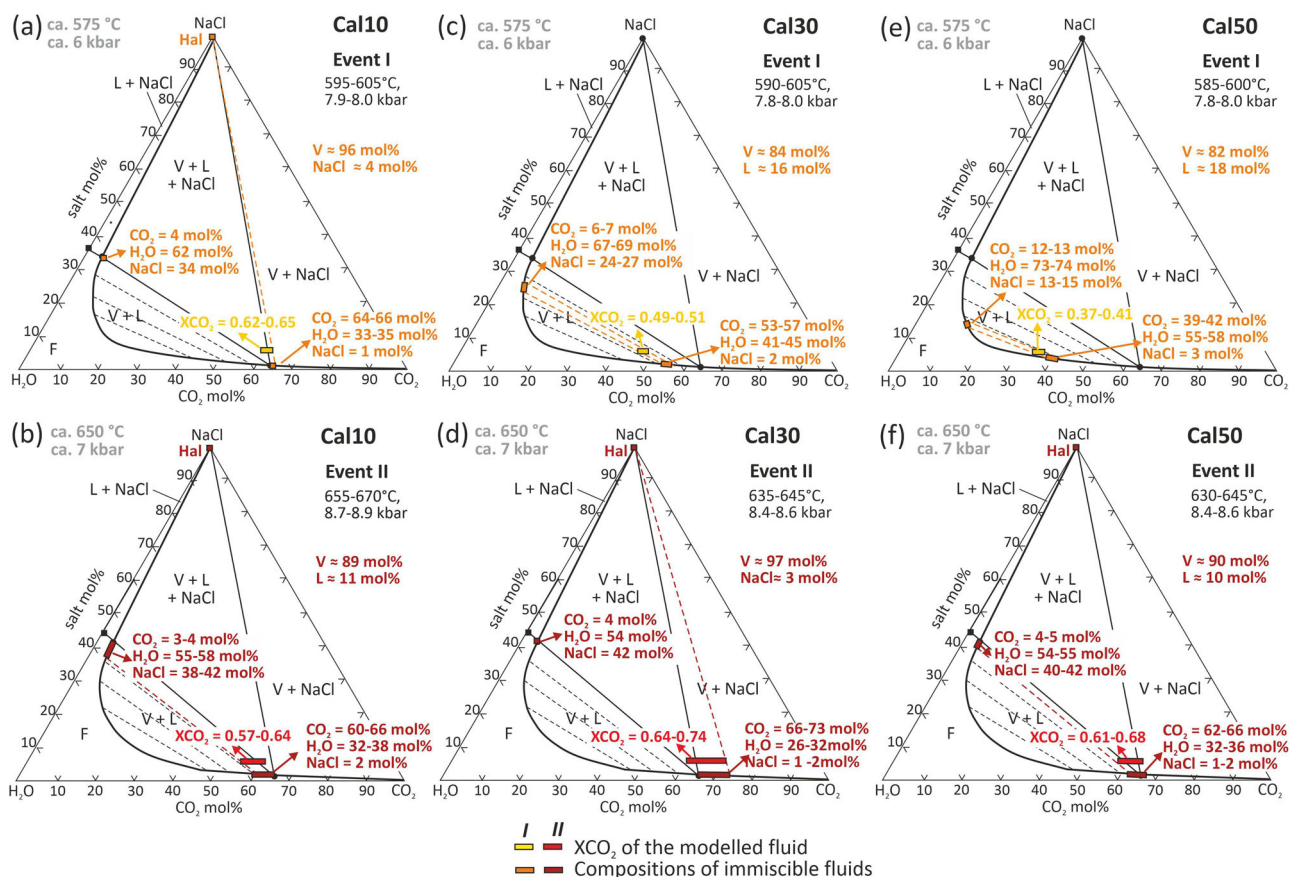


Fig. 3 Phase equilibria in the H₂O–CO₂–NaCl system. Phase equilibria in the H₂O–CO₂–NaCl system at ca. 575 °C, 5 kbar and at ca. 650 °C, 7 kbar (interpolated from experimental data by ref. ⁶⁹), showing phase relations for fluids generated by the modeled sediments (**a, b** Cal10; **c, d** Cal30; **e, f** Cal50) at the event I (**a, c, e**) and event II (**b, d, f**), in the hypothesis of salinity of 10 wt% NaCl (corresponding to NaCl ≈ 6–7 mol%). Dashed lines outline the V–L tie-lines within the two-phase fields. Depending on the bulk composition, fluids released during events I and II plot either within the *solvus* (**b, c, e, f**) or within the V + NaCl two-phase field (**a, d**). In the first case, two immiscible fluids coexist: a CO₂-rich vapor and a hydrosaline brine (boxes on the *solvus*), whereas in the second case, a CO₂-rich vapor coexists with halite. F one-phase fluid, V vapor, L liquid. Phase relations for Cal70 are reported in Supplementary Fig. S1a, b.

($X(\text{CO}_2) = 0.62\text{--}0.65$; Fig. 1b) plots within the V + NaCl two-phase field or in the nearby V + L + NaCl three-phase field. At these P – T conditions, a CO₂-rich vapor (CO₂ = 64–66 mol%; Table 2) coexists with halite, ± a very subordinate fraction of a hydrosaline brine (Fig. 3a). On the contrary, fluids produced by Cal30, Cal50, and Cal70 bulk compositions have lower $X(\text{CO}_2)$ values (Cal30: $X(\text{CO}_2) = 0.49\text{--}0.51$; Cal50: $X(\text{CO}_2) = 0.37\text{--}0.41$; Cal70: $X(\text{CO}_2) = 0.30\text{--}0.33$; Figs. 1d and 2b, d) and thus plot within the V + L two-phase field (Fig. 3c, e and Supplementary Fig. S1a), occasionally close to the boundary of the *solvus* (Cal50 and Cal70). Two immiscible fluids thus coexist also at these P – T conditions. The composition of conjugate fluids change as a function of the bulk-rock composition: specifically, the amount of CO₂ in the CO₂-rich vapor progressively decreases from Cal30 (CO₂ = 53–57 mol%) to Cal50 (CO₂ = 39–42 mol%) and Cal70 (CO₂ = 32–38 mol%) and the salinity of the brine decreases from Cal30 (NaCl = 24–27 mol%) to Cal50 (NaCl = 13–15 mol%) and Cal70 (NaCl = 11–12 mol%) (Table 2).

The topology of the ternary diagrams in the H₂O–CO₂–CaCl₂ system shows an even more extensive miscibility gap⁶⁹ at any P – T conditions (Fig. 4, Supplementary Fig. S1, and Table 3). Thus, fluids produced during events I and II constantly plot within the *solvus*, independent of the initial bulk-rock composition and even for extremely low C–O–H fluid salinities. Immiscible CO₂-rich vapor and a hydrosaline CaCl₂-rich brine are predicted for both events.

Therefore, carbonate-bearing sediments undergoing prograde metamorphic decarbonation reactions at relatively high temperatures and medium pressures release a conjugate fluid pair “born this way” (immiscible at the source; i.e., at a crustal depth of ~25–30 km), even for relatively low-salinity C–O–H initial fluid compositions (i.e., ≥5 wt% NaCl eq). In most cases, the CO₂-rich vapor is the dominant phase, coexisting with subordinate hydrosaline brines. Also, in the H₂O–CO₂–NaCl system, the coexistence of a vapor-like phase strongly enriched in CO₂ coexisting with halite is predicted. The immiscible CO₂-rich vapors produced during the most productive event II generally consist of more than 60 mol% CO₂ (up to 73 and 76 mol% in the NaCl and CaCl₂ systems, respectively) and are moderately saline, while hydrosaline brines generally contain > 60 wt% dissolved salt (i.e., close to saline melts; up to 69 wt% NaCl and 85 wt% CaCl₂).

Discussion

Implications for the CO₂ transport from the deep metamorphic source to the surface. Metamorphic C–O–H–salt fluids involved in dehydration and decarbonation reactions are generally modeled as a single phase. Fluid immiscibility has seldom been considered, although predicted by phase equilibria and documented by fluid inclusions, over different metamorphic environments and P – T – X conditions^{58,71–74}. The present results illustrate how decarbonation occurs within the *solvus*, generating immiscible CO₂-rich vapors and hydrosaline brines in the deep

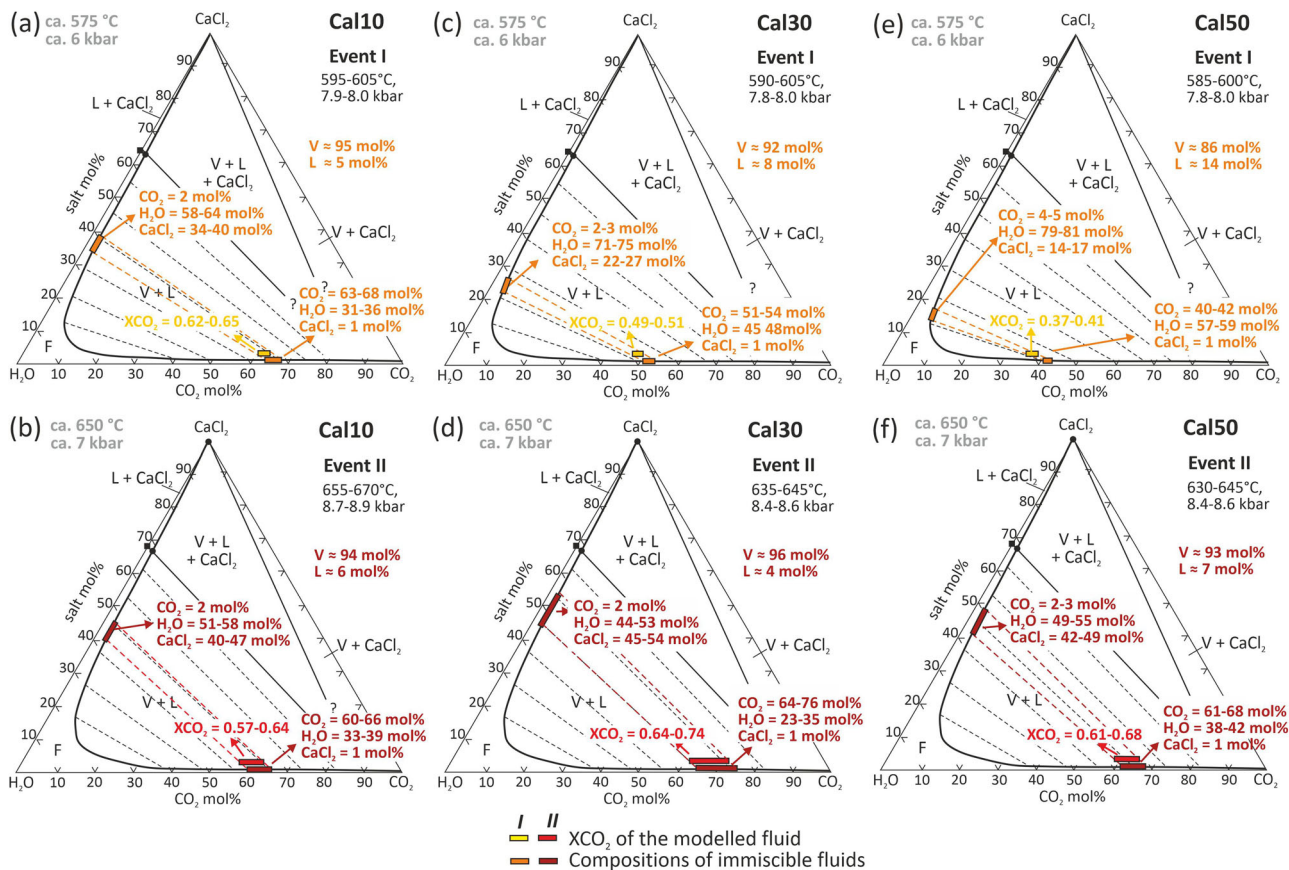


Fig. 4 Phase equilibria in the H₂O-CO₂-CaCl₂ system. Phase equilibria in the H₂O-CO₂-CaCl₂ system at ca. 575 °C, 5 kbar and at ca. 650 °C, 7 kbar (interpolated from experimental data by ref. 69), showing phase relations for fluids generated by the modeled sediments (a, b Cal10; c, d Cal30; e, f Cal50) at the event I (a, c, e) and event II (b, d, f), in the hypothesis of salinity of 10 wt% CaCl₂ (corresponding to CaCl₂ ≈ 3-4 mol%). Dashed lines outline the V-L tie-lines within the two-phase fields. Fluids released during events I and II systematically plot within the solvus. Two immiscible fluids thus coexist at every P-T conditions: a CO₂-rich vapor and a hydrosaline brine (boxes on the solvus). F one-phase fluid, V vapor, L liquid. Phase relations for Cal70 are reported in Supplementary Fig. S1c, d.

Table 2 Compositional ranges (mol%) of immiscible fluids generated by each modeled bulk composition (Cal10, Cal30, Cal50, Cal70) during event I and event II in the H₂O-CO₂-NaCl system.

Event I		Event II											
		Cal10		Cal30		Cal50		Cal70					
	V + L + S	V + S	V + L	V + L	V + L	V + L	V + L + S	V + S	V + L	V + L + S	V + L		
V	CO ₂	64	64-66	53-57	39-42	32-38	60-66	66	66	66-73	62-66	66	49-53
	H ₂ O	35	35-33	45-41	55-58	64-59	38-32	32	32	32-26	36-32	32	48-45
	NaCl	1	1	2	3	4-3	2	2	2	2-1	1-2	2	3-2
L	CO ₂	4	-	7-6	13-12	15-13	4-3	3	4	-	4-5	4	10-7
	H ₂ O	62	-	69-67	72-74	74-75	58-55	55	54	-	54-55	54	67-63
	NaCl	34	-	24-27	15-14	11-12	38-42	42	42	-	40-42	42	23-30
S	-	Hal	Hal	-	-	-	-	Hal	Hal	Hal	Hal	Hal	-

V vapor, L liquid (brine), S solid (salt).

crust of large hot orogens, at peak metamorphic conditions. Immiscibility favors fluid segregation allowing transport of carbon in the crust. Because of the density and viscosity contrast between coexisting fluids, significantly less dense CO₂-rich fluids (~1.06-1.10 g cm⁻³ 75,76) effectively separate from denser hydrosaline brines (~1.80 g cm⁻³), where most solutes concentrate, and migrate upwards. The contrasting wetting behavior and reactivity of CO₂ and brines further influence fluid migration from the deep crust. In silicate-dominated rocks, CO₂-rich fluids

have considerably higher dihedral angles ($\theta > 65^\circ$, up to 90°) compared to aqueous fluids, in which lower values are favored by the presence of alkali or alkaline-earth halides ($\theta < 40^\circ$) 77,78. In carbonate-dominated rocks, the behavior of CO₂-rich fluids is less obvious; low solid-fluid dihedral angles ($\theta < 60^\circ$), and therefore wetting properties, are observed for H₂O-CO₂ fluids with intermediate $X(\text{CO}_2)$ compositions ($0.2 < X(\text{CO}_2) < 0.6$), whereas H₂O-rich fluids ($X(\text{CO}_2) < 0.2$) and CO₂-rich fluids with $X(\text{CO}_2) > 0.6$ have high dihedral angles ($\theta > 65^\circ$, up to 90°) and

Table 3 Compositional ranges (mol%) of immiscible fluids generated by each modeled bulk composition (Cal10, Cal30, Cal50, Cal70) during event I and event II in the H₂O-CO₂-CaCl₂ system.

Event I						Event II					
		V + L Cal10	V + L Cal30	V + L Cal50	V + L Cal70			V + L Cal10	V + L Cal30	V + L Cal50	V + L Cal70
V	CO ₂	63–68	51–54	40–42	32–39	V	CO ₂	60–66	64–76	61–68	48–54
	H ₂ O	36–31	48–45	59–57	66–59		H ₂ O	39–33	35–23	42–38	51–45
	CaCl ₂	1	1	1	2		CaCl ₂	1	1	1	1
L	CO ₂	2	3–2	5–4	7–6	L	CO ₂	2	2	3–2	4–3
	H ₂ O	64–58	75–71	81–79	83–82		H ₂ O	58–51	53–44	55–49	68–64
	CaCl ₂	34–40	22–27	14–17	10–12		CaCl ₂	40–47	45–54	42–49	28–33
S	–	–	–	–	–	S	–	–	–	–	–

V vapor, L liquid (brine), S solid (salt).

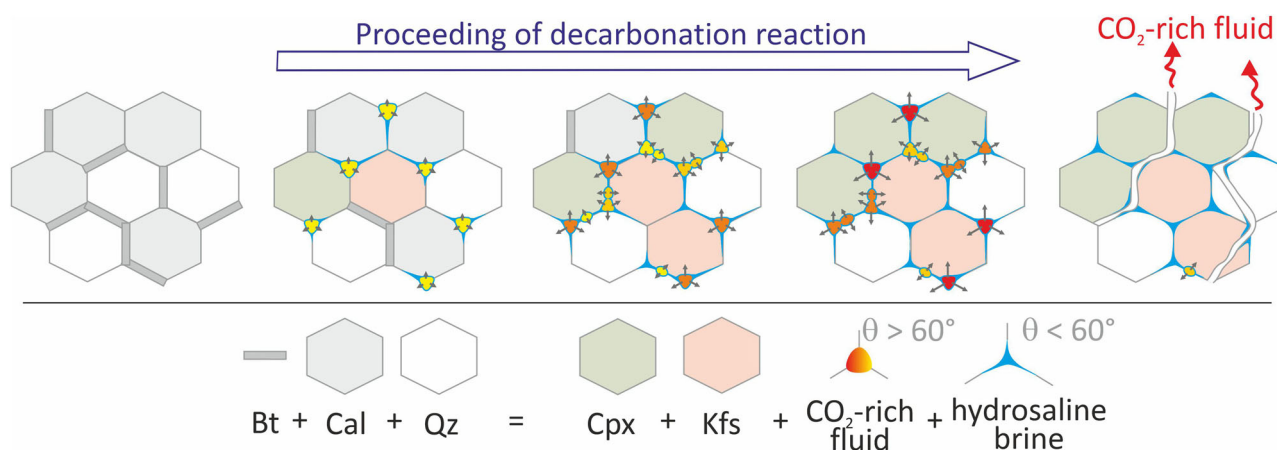


Fig. 5 Sketch illustrating fluid production and evolution at the proceeding of a decarbonation reaction ($Bt + Cal + Qz = Cpx + Kfs + \text{fluid}$), which occurs at a depth of 25–30 km (i.e., at P - T conditions compatible with event II). Two immiscible fluids are generated in the source rocks: the CO₂-rich fluid is shown in yellow-red, with colors changing from yellow to red according to the progressive increase of the fluid pressure within the pores, whereas the hydrosaline brine is reported in blue. The short to long black arrows radiating from the CO₂-filled pores indicate the progressive increase of the fluid pressure in the pores. The dihedral angles of the two fluids (CO₂-rich fluid: $\theta > 60^\circ$; hydrosaline brine: $\theta < 60^\circ$) imply that the CO₂-rich fluid accumulates within isolated fluid pockets, whereas the hydrosaline brine forms thin interconnected films along grain edges. As far as the decarbonation reaction proceeds, fluid pressure within the CO₂-rich pockets increases until fluid overpressure is reached, carbo-fracturing the host rocks. The CO₂-rich fluid thus rapidly escapes toward the surface along the newly created fracture network, whereas the denser, hydrosaline brine remains trapped in the source rock.

therefore they are non-wetting fluids⁷⁹. Therefore, CO₂-rich fluids generated during events I and II mostly have a non-wetting behavior (except in carbonate-dominated lithologies, i.e., Cal70, whose CO₂ productivity is so low that they will not be further considered in the discussion). Thus, it is conceivable that the less dense CO₂-rich fluids are highly buoyant and unreactive, whereas the volumetrically minor and denser hydrosaline brines are highly reactive and could migrate by porous flow through thin interconnected films along grain boundaries⁷⁷ (Fig. 5). Our results also suggest that a solid salt instead of a brine could be segregated from a single CO₂-rich vapor-like phase for specific rock and fluid compositions.

Thus, in a two-fluid flow regime, CO₂ and brines migrate separately. CO₂-rich fluids generated at depths of 25–30 km (8–10 kbar) would accumulate, eventually forming large reservoirs. With decarbonation reactions proceeding, confined CO₂-rich fluids would cause fluid overpressure, inducing carbo-fracturing of the host rocks and migrating upward. Such processes could trigger crustal permeability, possibly resulting in earthquake nucleation and seismicity^{28,80–85}. An alternative scenario of a passive ascent of CO₂-rich fluids, favored by brittle fracturing of the crust during earthquakes or by ductile

deformation, could be equally possible to enhance fluid mobility through channelization along preferential pathways. In both cases, fracturing and faulting would allow fast CO₂-rich fluids migration toward the surface^{28,81,82,85–88}. As CO₂-rich fluids are removed from the reacting sites, the remaining hypersaline brines could represent important metasomatic agents in the lower crust^{48,58,89}. Moreover, their low water activity could promote granulitization of the deep crust, delaying its partial melting.

Fluid-rock interaction during ascent is unlikely because the relatively high transport velocities and the nonpolar nature of CO₂-rich fluids do not allow chemical equilibration with most metamorphic rock compositions. To our knowledge, pervasive carbonation by fluid-rock interactions at P - T conditions compatible with fluid ascent in large hot orogenic settings is limited to soapstones, listvenites and sagvandites (i.e., talc + magnesite, quartz + magnesite and enstatite + magnesite rocks derived from ultramafic lithologies by reaction with a CO₂-rich fluid^{90–97}). However, ultramafic lithologies are rare in large hot orogens and are regarded as exceptions rather than rules. Also, precipitation of epigenetic graphite should be negligible due to the low water activity in CO₂-rich fluids coupled with the high temperatures at which decarbonation reactions occur⁹⁸.

Fluid immiscibility supports geochemical and geophysical observations from active large hot orogens. Segregation of CO₂-rich fluids by phase separation at birth (i.e., directly in the deep crustal source) reconciles geochemical and geophysical evidence from active collisional orogens, e.g., the Himalaya, considered as the archetype of large hot orogens and characterized by present-day intense CO₂ surface degassing.

First, immiscibility, with the generation of CO₂-dominated fluids (i.e., $X(\text{H}_2\text{O}) = 26\text{--}38\text{ mol}\%$), could explain the gaseous CO₂ emissions measured at the surface. Diffuse degassing occurs over extensive areas in Himalaya, testified by the widespread occurrence of CO₂-rich hot springs and gaseous CO₂ ground discharges along the main tectonic discontinuities and distributed along the entire length of the orogenic belt^{9,27,28,85,99,100}. Geochemical and isotopic analyses revealed that CO₂ released at the surface has a crustal metamorphic signature, produced at >5 km depth^{9,27,28,85,100}. Girault & Perrier⁸⁴ and Girault et al.⁸⁸ suggested that CO₂ is not dissolved in aqueous fluids but, instead, rapidly outgas along “dry” faults toward the surface. Estimated transport velocities are in the order of 0.1 to 1 m sec⁻¹ to account for the observed radon and CO₂ fluxes.

Second, beneath the Himalayan metamorphic core, a major conductive zone is revealed at a depth of ~20–30 km¹⁰¹, immediately below a zone of intense microseismicity^{102–104}. This highly conductive and seismically active zone is located along a mid-crustal ramp below the superficial emergence of the Main Central Thrust (Fig. 6), i.e., the main tectonic discontinuity along which most of the CO₂-rich hot springs are concentrated. Lemonnier et al.¹⁰¹ first interpreted the conductivity anomaly as related to highly connected aqueous fluids released by metamorphic dehydration reactions, percolating upward into the brittle portion of the crust, where microseismic activity is observed. In aqueous fluids, conductivity is low but readily increases with salinity¹⁰⁵. Thus, this deep conductive zone could result from the stagnation of hydrosaline brines⁴⁸ left behind by the CO₂-rich fluids once they rise toward the surface. Although volumetrically minor, hydrosaline brines have an extremely wetting behavior¹⁰⁶. It is, therefore, likely that they are highly connected in the source rocks (Fig. 5). Like Lemonnier et al.¹⁰¹ original interpretation, the zone of intense microseismicity immediately above the conductive anomaly could be related to periodic carbo-fracturing events in the brittle crust induced by the accumulation of CO₂-rich fluids at the lower crust–upper crust boundary. Finally, given the striking similarities between actual

CO₂ fluxes measured at the surface and those predicted by modeling of prograde metamorphism of carbonate-bearing lithologies in Himalaya at depths of 25–30 km (i.e., at 650–750 °C, 8–10 kbar^{24,25,31,38}), it seems likely that CO₂-producing processes and transport mechanisms similar to those occurring in Himalaya at present were also active in the past.

In conclusion, we demonstrate that the most productive CO₂-source rocks in large hot orogens are calcareous pelites and carbonate-poor marls (i.e., Cal10 and Cal30), which generate immiscible CO₂-rich fluids and hydrosaline brines when metamorphosed at $T > 590\text{ °C}$. We suggest that fluid immiscibility provides a physical mechanism to transport carbon liberated during prograde metamorphism. Segregation due to density contrast and different chemical properties between CO₂ and brines allows the rapid migration of CO₂ from the deep source to the surface. Such a model could explain the CO₂ fluxes currently measured at the surface in active collisional orogenic settings such as the Himalaya, which are impossible to explain in the absence of fluid phase separation. Finally, our study contributes to solving the debate on the role of orogenic settings for the global Earth's CO₂ tectonic outgassing. An array of independent observations consistently indicates that active collisional orogens could represent an important (and so far under-considered) source of CO₂ on a global scale. Since the Himalayan orogen is a modern analog of ancient large hot orogens, such as the Mesoproterozoic Grenville and Sveconorwegian orogens and the Late Palaeozoic Variscan orogen, we advocate that the same process currently active in the Himalaya should have been repeatedly active at different times, during the main orogenic events, possibly causing periodic perturbations of the atmospheric CO₂ levels.

Methods

Model bulk-rock compositions. Model bulk-rock compositions used to calculate the P/T - $X(\text{CO}_2)$ buffering paths were obtained by adding 10, 30, 50, and 70 vol% of calcite to the average pelite composition of ref. ³⁴ (“shale and slate” group; his Table 2) (Table 1). The modal proportions of the protolith's minerals have been obtained by applying the least square method (freeware application available on demand¹⁰⁷) and using end-member compositions and molar volumes for kaolinite, illite, clinocllore, daphnite, albite, anorthite, quartz, and K-feldspar. The result is considered satisfactory if the residuals (i.e., molar bulk composition of the protolith's minerals—molar bulk-rock composition) is close to zero. The following assumptions were additionally made: (a) CaO from silicate fraction is equivalent to Na₂O^{108,109} and is incorporated in anorthite; the remaining CaO is incorporated in calcite; (b) chlorite is the only Fe-Mg mineral in the protolith and (c) albite incorporates all the Na₂O.

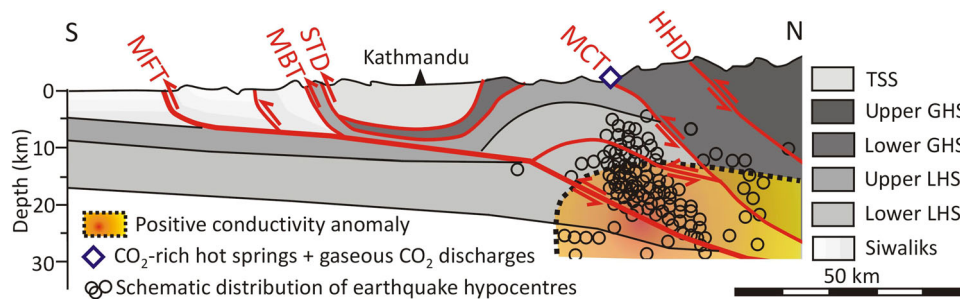


Fig. 6 Schematic geologic section across central Nepal Himalaya at the longitude of Kathmandu. The thick red line shows the Main Himalayan Thrust, MHT, which reaches the surface at the front of the Siwalik Hills, coinciding with the Main Frontal Thrust (MFT). The Main Boundary Thrust (MBT) separates the metasediments of the Lesser Himalayan Sequence (LHS) from the molasse deposits of the sub-Himalaya (the Siwaliks Hills). The Main Central Thrust (MCT) places the higher-grade metamorphic rocks of the Greater Himalayan Sequence (GHS) over the LHS metasediments. The GHS is divided into two tectono-metamorphic units (Lower-GHS and Upper-GHS) by the High Himalayan Discontinuity (HHD); geologic cross-section modified from refs. ^{104,122}. The red to yellow area highlights the zone of high conductivity located at depths >15 km beneath the superficial emergence of the MCT, as obtained from the magnetotelluric experiment of ref. ¹⁰¹. The conductivity anomaly is associated with intense microseismic activity, evidenced by the schematic distribution of earthquake hypocentres (small circles). The white diamond indicates the CO₂-rich hot springs and gaseous CO₂ discharges from the ground, located along the MCT.

Thermodynamic modeling. Thermodynamic modeling was performed using PerpleX 6.9.0^{110,111} (version June 2020), the internally consistent thermodynamic dataset (version ds55), and the equation of state for H₂O–CO₂ binary fluid of ref. ¹¹². P/T - $X(\text{CO}_2)$ buffering paths were calculated along a P/T geothermal gradient representative of large hot orogens ($dT/dP = 750 \text{ }^\circ\text{C GPa}^{-1}$ (see ref. ³⁵)). The following solution models were considered: carbonate (i.e., Ca–Mg–Mn–Fe carbonate with calcite structure¹¹³), dolomite¹¹², scapolite¹¹⁴, chlorite¹¹⁵, white mica^{116,117}, biotite¹¹⁸, plagioclase¹¹⁹, K-feldspar¹²⁰, Ca-amphibole (ideal tremolite solution model), clinopyroxene¹¹², garnet¹¹², epidote¹¹², chloritoid¹¹², and staurolite¹¹². A generic hybrid molecular fluid-equation-of-state solution model was used for fluid (COH-Fluid model available in PerpleX), including H₂O, CO₂, CO, CH₄, and H₂ molecular species. This model allows considering redox processes, such as the possible reduction of carbon to graphite due to the exchange of oxygen between the C–O–H fluid and the Fe³⁺-bearing solid phases (white mica, biotite, clinopyroxene, garnet, epidote).

Calculation of P/T - $X(\text{CO}_2)$ buffering paths requires fixing a P - T - $X(\text{CO}_2)$ starting condition; this was fixed at 350 °C, 4 kbar, $X(\text{CO}_2) = 0.005$, such as the predicted mineral modes are as close as possible to the calculated protolith's mineral modes (with muscovite replacing illite). The Werami routine of Perple_X was used to calculate the amount of H₂O, C, and O₂ stored in solid phases at the starting P - T - $X(\text{CO}_2)$ fluid-saturated conditions (Cal10_0, Cal30_0, Cal50_0, and Cal70_0 compositions in Supplementary Tables S1–4). To start calculating the buffering paths, 1 mol% of the equilibrium fluid with $X(\text{CO}_2) = 0.005$ was added to each model bulk-rock composition (Cal10_1, Cal30_1, Cal50_1, Cal70_1 compositions in Supplementary Tables S1–4). The addition of a small amount of fluid is required because, at fluid saturation conditions, the Werami routine returns the amounts of H₂O, C, and O₂ stored in minerals, but not the amount of free fluid in equilibrium with solid phases, which in turn depends on the porosity of the system (see ref. ¹²¹ for further details). P/T - $X(\text{CO}_2)$ buffering paths were calculated following the constant porosity model of ref. ¹²¹. According to this model, the fluid is allowed to accumulate within the rock until it reaches a specified molar proportion threshold; each time this threshold is exceeded, fluid loss occurs through a stepwise process. Starting from the initial fluid mole proportion of 0.01 (1 mol%, relative to the solids + fluid assemblage), we have fixed the threshold at 0.02; this implies that when the fluid proportion reaches this value, its amount is reduced to 0.01. Bulk compositions after each fractionation step are reported in Supplementary Tables S1–4. Supplementary Tables S1–4 also include the modeled amounts of fluid (vol%, relative to the solids + fluid assemblage) immediately before and immediately after each fractionation step, and show that fractionation of fluid allows maintaining a porosity <2 vol%. The two extreme cases of an internally buffered, completely closed system (i.e., no fluid loss is allowed) and of an internally buffered completely open system (i.e., all the fluid that is produced is immediately lost) were further considered, which provide the minimum and maximum $X(\text{CO}_2)$ values, respectively, for the same starting conditions.

Figures 1 and 2 show the variations in mineral proportions (vol%, fluid excluded), the loss (wt%) of CO₂ and H₂O relative to the initial CO₂ and H₂O content in the solids, and the composition ($X(\text{CO}_2)$ = molar fraction of CO₂) of the fluid released along the calculated buffering paths. The complete speciation of the fluid along the modeled buffering paths is reported in Supplementary Data Files S1–4.

Estimate of the amounts of CO₂ and H₂O released along the modeled prograde P/T - $X(\text{CO}_2)$ buffering paths. The Werami routine of Perple_X was used to infer: (i) the abundances (wt%) of both C-bearing minerals (carbonates and scapolite) and hydrous minerals (chlorite, muscovite, biotite, epidote) along the calculated P/T - $X(\text{CO}_2)$ buffering paths, (ii) the amounts (wt%) of C, O₂, and H₂O hosted in these minerals at each P - T conditions. Although scapolite can incorporate significant amounts of Cl in compositions close to the marialite end-member, it is to be noted that in the available scapolite solution model¹¹⁴ marialite is treated as a hypothetical CO₃ end-member. This would potentially result in an overestimation of the CO₂ content in scapolite. However, this should not significantly influence the final estimate of CO₂ production because available data on natural scapolite from large hot orogenic contexts suggest that most scapolite contain negligible (if not null) amounts of Cl^{24,25}. The amounts (wt%) of CO₂ and H₂O released during prograde metamorphism from each model bulk composition were then calculated by adding carbonates' contribution with that of scapolite and chlorite's contribution with that of muscovite, biotite, and epidote, respectively. Supplementary Data Files S1–4 summarize the variations in mineral proportions (vol% and wt%) and the amounts (wt%) of C, O₂, and H₂O released along the calculated buffering paths and used for Figs. 1 and 2.

Data availability

The authors declare that all data supporting the findings of this study are available within the article (Tables 1–3) and its Supplementary Information files (Supplementary Tables S1–S4 and Supplementary Data Files S1–S4). The thermodynamic database and solution models used for thermodynamic modeling are available on the Perple_X website (<https://www.perpleX.ethz.ch/>).

Code availability

No computer code was written in preparing the paper. The Perple_X code used for the thermodynamic modeling (Perple_X 6.9.0, version June 2020) is available on the Perple_X website (<https://www.perpleX.ethz.ch/>).

Received: 30 April 2021; Accepted: 15 December 2021;

Published online: 18 January 2022

References

- Flesia, C. & Frezzotti, M. L. The dilemma of the dwarf Earth's CO₂ degassing: irrelevant or crucial? *J. Geochem. Explor.* **152**, 118–122 (2015).
- Bowen, N. L. Progressive metamorphism of siliceous limestone and dolomite. *J. Geol.* **48**, 225–274 (1940).
- Ferry, J. M. Regional metamorphism of the Waits River Formation, eastern Vermont: delineation of a new type of giant metamorphic hydrothermal system. *J. Petrol.* **33**, 45–94 (1992).
- Bickle, M. J. Metamorphic decarbonation, silicate weathering and the long-term carbon cycle. *Terra Nova* **8**, 270–276 (1996).
- Kerrick, D. M. & Caldeira, K. Metamorphic CO₂ degassing from orogenic belts. *Chem. Geol.* **145**, 213–232 (1998).
- Ague, J. J. Release of CO₂ from carbonate rocks during regional metamorphism of lithologically heterogeneous crust. *Geology* **28**, 1123–1126 (2000).
- Stewart, E. M. et al. Carbonation and decarbonation reactions: implications for planetary habitability. *Am. Mineral.* **104**, 1369–1380 (2019).
- Kerrick, D. M. & Caldeira, K. Was the Himalayan orogen a climatically significant coupled source and sink for atmospheric CO₂ during the Cenozoic? *Earth Planet. Sci. Lett.* **173**, 195–203 (1999).
- Becker, J. A., Bickle, M. J., Galy, A. & Holland, T. J. B. Himalayan metamorphic CO₂ fluxes: quantitative constraints from hydrothermal springs. *Earth Planet. Sci. Lett.* **265**, 616–629 (2008).
- Gaillardet, J. & Galy, A. Himalaya-carbon sink or source? *Science* **320**, 1727–1728 (2008).
- Evans, K. A. Metamorphic carbon fluxes: how much and how fast? *Geology* **39**, 95–96 (2011).
- Hazen, R. M. & Schiffries, C. M. Why deep carbon? *Rev. Mineral. Geochem.* **75**, 4–6 (2013).
- Skelton, A. D. L., Bickle, M. J. & Graham, C. M. Fluid-flux and reaction rate from advective-diffusive carbonation of mafic sill margins in the Dalradian, southwest Scottish Highlands. *Earth Planet. Sci. Lett.* **146**, 527–539 (1997).
- Skelton, A. D. L. Flux rates for water and carbon during greenschist facies metamorphism. *Geology* **39**, 43–46 (2011).
- Kleine, B. I., Pitcairn, I. K. & Skelton, A. D. The mechanism of infiltration of metamorphic fluids recorded by hydration and carbonation of epidote–amphibole facies metabasaltic sills in the S.W. Scottish Highlands. *Am. Mineral.* **100**, 2702–2717 (2015).
- Kleine, B. I., Pitcairn, I. K. & Skelton, A. D. Mineralogical controls on metamorphic fluid flow in metabasaltic sills from Islay, Scotland. *Lithos* **248**, 22–39 (2016).
- Kleine, B. I., Zhao, Z. & Skelton, A. Rapid fluid flow along fractures at greenschist facies conditions on Syros, Greece. *Am. J. Sci.* **316**, 169–201 (2016).
- Piccoli, F. et al. Carbonation by fluid–rock interactions at high-pressure conditions: implications for carbon cycling in subduction zones. *Earth Planet. Sci. Lett.* **445**, 146–159 (2016).
- Menzel, M. D. et al. Carbonation of mantle peridotite by CO₂-rich fluids: the formation of listvenites in the Advocate ophiolite complex (Newfoundland, Canada). *Lithos* **323**, 238–261 (2018).
- Peng, W. et al. Multistage CO₂ sequestration in the subduction zone: Insights from exhumed carbonated serpentinites, SW Tianshan UHP belt, China. *Geochim. Cosmochim. Acta* **270**, 218–243 (2020).
- Hu, H. et al. Retrograde carbon sequestration in orogenic complexes: a case study from the Chinese southwestern Tianshan. *Lithos* **392–393**, 106151 (2021).
- Groppo, C., Rolfo, F., Castelli, D. & Connolly, J. A. D. Metamorphic CO₂ production from calc-silicate rocks via garnet-forming reactions in the CFAS–H₂O–CO₂ system. *Contrib. Mineral. Petrol.* **166**, 1655–1675 (2013).
- Craw, D. & Upton, P. Graphite reaction weakening of fault rocks, and uplift of the Annapurna Himal, central Nepal. *Geosphere* **10**, 720–731 (2014).
- Groppo, C., Rolfo, F., Castelli, D. & Mosca, P. Metamorphic CO₂ production in collisional orogens: petrologic constraints from phase diagram modeling of Himalayan, scapolite-bearing, calc-silicate rocks in the NKC(F)MAS(T)–HC system. *J. Petrol.* **58**, 53–83 (2017).
- Rapa, G. et al. Titanite-bearing calc-silicate rocks constrain timing, duration and magnitude of metamorphic CO₂ degassing in the Himalayan belt. *Lithos* **292–293**, 364–378 (2017).
- Stewart, E. M. & Ague, J. J. Infiltration-driven metamorphism, New England, USA: regional CO₂ fluxes and implications for Devonian climate and extinctions. *Earth Planet. Sci. Lett.* **489**, 123–134 (2018).
- Perrier, F. et al. A direct evidence for high carbon dioxide and radon-222 discharge in Central Nepal. *Earth Planet. Sci. Lett.* **278**, 198–207 (2009).

28. Girault, F. et al. The Syabru-Bensi hydrothermal system in central Nepal: 1. characterization of carbon dioxide and radon fluxes. *Geophys. Res. Solid Earth* **119**, 4017–4055 (2014).
29. Beaumont, C., Nguyen, M. H., Jamieson, R. A. & Ellis, S. Crustal flow modes in large hot orogens. In *Channel Flows, Ductile Extrusion and Exhumation in Continental Collision Zones* (eds Law, R. D., Searle, M. P. & Godin, L.) Vol. 268, 91–145 (Geological Society Special Publication, 2006).
30. Beaumont, C., Jamieson, R. & Nguyen, M. Models of large, hot orogens containing a collage of reworked and accreted terranes. *Can. J. Earth Sci.* **47**, 485–515 (2010).
31. Groppo, C., Rapa, G., Frezzotti, M. L. & Rolfo, F. The fate of calcareous pelites in collisional orogens. *J. Metam. Geol.* **39**, 181–207 (2021).
32. Greenwood, H. J. Buffering of pore fluids by metamorphic reactions. *Am. J. Sci.* **275**, 573–593 (1975).
33. Baker, J., Holland, T. J. B. & Powell, R. Isograds in internally buffered systems without solid solutions: principles and examples. *Contrib. Mineral. Petrol.* **106**, 170–182 (1991).
34. Ague, J. J. Evidence for major mass transfer and volume change during regional metamorphism of pelites. *Geology* **19**, 855–858 (1991).
35. Brown, M. Duality of thermal regimes is the distinctive characteristic of plate tectonics since the Neoproterozoic. *Geology* **34**, 961–964 (2016).
36. Morissey, L. J. & Tomkins, A. G. Evaporite-bearing orogenic belts produce ligand-rich and diverse metamorphic fluids. *Geochim. Cosmochim. Acta* **275**, 163–187 (2020).
37. Yardley, B. W. D. The Evolution of Fluids through the metamorphic cycle. In *Fluid Flow and Transport in Rocks* (eds Jamveit, B. & Yardley, B. W. D.) 99–121 (Springer, 1997).
38. Rolfo, F., Groppo, C. & Mosca, P. Metamorphic CO₂ production in calc-silicate rocks from the eastern Himalaya. *It. J. Geosci.* **136**, 28–38 (2017).
39. Pêcher, A. Les inclusions fluides des quartz d'exsudation de la zone du MCT himalayen au Népal central: données sur la phase fluide dans une grande zone de cisaillement crustal. *Bull. Minéral.* **102**, 537–554 (1979).
40. Sisson, V. B. & Hollister, L. S. A fluid-inclusion study of metamorphosed pelitic and carbonate rocks, south central Maine. *Am. Mineral.* **75**, 59–70 (1990).
41. Sisson, V. B., Crawford, M. L. & Thompson, P. H. CO₂-brine immiscibility at high temperatures: evidence from calcareous metasedimentary rocks. *Contrib. Mineral. Petrol.* **78**, 371–378 (1981).
42. Carmichael, D. M. Univariant mixed-volatile reactions: pressure-temperature phase diagrams and reaction isograds. *Can. Mineral.* **29**, 741–754 (1991).
43. Connolly, J. A. D. & Trommsdorff, V. Petrogenetic grids for metacarbonate rocks: pressure-temperature phase-diagram projection for mixed-volatile systems. *Contrib. Mineral. Petrol.* **108**, 93–105 (1991).
44. Yardley, B. W. D. & Shmulovich, K. I. An introduction to crustal fluids. In *Fluids in The Crust: Equilibrium and Transport Properties* (eds Shmulovich, K. I., Yardley, B. W. D. & Gonchar, G. G.) 1–12 (Chapman & Hall, 1995).
45. Castelli, D., Rolfo, F., Groppo, C. & Compagnoni, R. Impure marbles from the UHP Brossasco-Isasca Unit (Dora-Maira Massif, Western Alps): evidence for Alpine equilibration in the diamond stability field and evaluation of the X(CO₂) fluid evolution. *J. Metam. Geol.* **25**, 587–603 (2007).
46. Yardley, B. W. D. & Graham, J. T. The origins of salinity in metamorphic fluids. *Geofluids* **2**, 249–256 (2002).
47. Yardley, B. W. D. & Bodnar, R. J. Fluids in the continental crust. *Geochem. Perspect.* **3**, 1–123 (2014).
48. Manning, C. E. Fluids of the lower crust: deep is different. *Annu. Rev. Earth Planet. Sci.* **46**, 67–97 (2018).
49. Evans, K. A. & Tomkins, A. G. Metamorphic fluids in orogenic settings. *Elements* **16**, 381–388 (2020).
50. Rowan, M. G. Passive-margin salt basins: hyperextension, evaporite deposition, and salt tectonics. *Basin Res.* **26**, 154–182 (2014).
51. Xie, F. et al. Passive continental margin basins and the controls on the formation of evaporites: a case study of the Gulf of Mexico Basin. *Carbonates Evaporites* **34**, 405–418 (2019).
52. Warren, J. K. Evaporites, brines and base metals: fluids, flow and “the evaporite that was”. *Australian J. Earth Sci.* **44**, 149–183 (1997).
53. Warren, J. K. *Evaporites: Sediments, Resources and Hydrocarbons* (Springer-Verlag, 2006).
54. Markl, G. & Bucher, K. Composition of fluids in the lower crust inferred from metamorphic salt in lower crustal rocks. *Nature* **391**, 781–783 (1998).
55. Newton, R. C., Aranovich, L. Y., Hansen, E. C. & Vandenheuvell, B. A. Hypersaline fluids in Precambrian deepcrustal metamorphism. *Precambrian Res.* **91**, 41–63 (1998).
56. Touret, J. L. R. Fluid regime in southern Norway: the record of fluid inclusions. In *The Deep Proterozoic Crust in the North Atlantic Provinces* (eds Tobi, A. C. & Touret, J. L. R.) 517–549 (Reidel, 1985).
57. Trommsdorff, V., Skippen, G. & Ulmer, P. Halite and sylvite as solid inclusions in high-grade metamorphic rocks. *Contrib. Mineral. Petrol.* **89**, 24–29 (1985).
58. Heinrich, W. Fluid immiscibility in metamorphic rocks. *Rev. Mineral. Geochem.* **65**, 389–430 (2007).
59. Liebscher, A. Aqueous fluids at elevated pressure and temperature. *Geofluids* **10**, 3–19 (2010).
60. Manning, C. E. & Aranovich, L. Y. Brines at high pressure and temperature: thermodynamic, petrologic and geochemical effects. *Precambrian Res.* **253**, 6–16 (2014).
61. Manning, C. E. & Frezzotti, M. L. Subduction-Zone fluids. *Elements* **16**, 395–400 (2020).
62. Trommsdorff, V. & Skippen, G. Vapour loss (“boiling”) as a mechanism for fluid evolution in metamorphic rocks. *Contrib. Mineral. Petrol.* **94**, 317–322 (1986).
63. Skippen, G. & Trommsdorff, V. The influence of NaCl and KCl on phase relations in metamorphosed carbonate rocks. *Amer. J. Sci.* **286**, 81–104 (1986).
64. Heinrich, W., Churakov, S. S. & Gottschalk, M. Mineral-fluid equilibria in the system CaO-MgO-SiO₂-H₂O-CO₂-NaCl and the record of reactive fluid flow in contact metamorphic aureoles. *Contrib. Mineral. Petrol.* **148**, 131–149 (2004).
65. Crawford, M. L., Kraus, D. W. & Hollister, L. S. Petrologic and fluid inclusion study of calc-silicate rocks, Prince Rupert, British Columbia. *Amer. J. Sci.* **279**, 1135–1159 (1979).
66. Zhang, Y. G. & Frantz, J. D. Experimental determination of the compositional limits of immiscibility in the system CaCl₂-H₂O-CO₂ at high temperatures and pressures using fluid inclusions. *Chem. Geol.* **74**, 289–308 (1989).
67. Shmulovich, K. I. & Plyasunova, N. V. Phase equilibria in ternary systems formed by H₂O and CO₂ with CaCl₂ or NaCl at high T and P. *Geochem. Internat.* **30**, 53–71 (1993).
68. Shmulovich, K. I., Tkachenko, S. I. & Plyasunova, N. V. Phase equilibria in fluid systems at high pressures and temperatures. In *Fluids in the Crust* (eds Shmulovich, K. I., Yardley, B. W. D. & Gonchar, G. G.) 193–214 (Chapman and Hall, 1995).
69. Shmulovich, K. I. & Graham, C. M. An experimental study of phase equilibria in the systems H₂O-CO₂-CaCl₂ and H₂O-CO₂-NaCl at high pressures and temperatures (500–800 °C, 0.5–0.9 GPa): geological and geophysical applications. *Contrib. Mineral. Petrol.* **146**, 450–462 (2004).
70. Duan, Z., Møller, N. & Weare, J. H. Equation of state for the NaCl-H₂O-CO₂ system: prediction of phase equilibria and volumetric properties. *Geochem. Cosmochim. Acta* **59**, 2869–2882 (1995).
71. Yardley, B. W. D. & Bottrell, S. H. Immiscible fluids in metamorphism: implications of two-phase fluid flow for reaction history. *Geology* **16**, 199–202 (1988).
72. Frezzotti, M. L. & Touret, J. L. R. CO₂, carbonate-rich melts, and brines in the mantle. *Geosci. Front.* **5**, 697–710 (2014).
73. Frezzotti, M. L. & Ferrando, S. The chemical behavior of fluids released during deep subduction based on fluid inclusions. *Am. Mineral.* **100**, 352–377 (2015).
74. Li, Y. Immiscible C-O-H fluids formed at subduction zone conditions. *Geochem. Perspect. Lett.* **3**, 12–21 (2017).
75. Bower, T. S. & Hegelson, H. C. Calculation of the thermodynamic and geochemical consequences of non-ideal mixing in the system H₂O-CO₂-NaCl on phase relations in geological systems: equation of state for H₂O-CO₂-NaCl fluids at high pressures and temperatures. *Geochim. Cosmochim. Acta* **47**, 1247–1275 (1983).
76. Bakker, R. J. Package FLUIDS 1. Computer programs for analysis of fluid inclusion data and for modelling bulk fluid properties. *Chem. Geol.* **194**, 3–23 (2003).
77. Watson, E. B. & Brenan, J. M. Fluid in the lithosphere. I. experimentally determined wetting characteristics of CO₂-H₂O fluids and their implications for fluid transport, host-rock physical properties, and fluid inclusion formation. *Earth Planet. Sci. Lett.* **85**, 497–515 (1987).
78. Holness, M. B. Equilibrium dihedral angles in the system quartz-CO₂-H₂O-NaCl at 800 °C and 1–15 kbar: the effects of pressure and fluid composition on the permeability of quartzites. *Earth Planet. Sci. Lett.* **114**, 171–184 (1992).
79. Holness, M. B. & Graham, C. M. Equilibrium dihedral angles in the system CO₂-H₂O-NaCl-calcite, and implications for fluid flow during metamorphism. *Contrib. Mineral. Petrol.* **108**, 368–383 (1991).
80. Irwing, W. P. & Barnes, I. Tectonic relations of carbon dioxide discharges and earthquakes. *J. Geophys. Res.* **85**, 3115 (1980).
81. Chiodini, G. et al. Carbon dioxide Earth degassing and seismogenesis in central and southern Italy. *Geophys. Res. Lett.* **31**, 2–5 (2004).
82. Chiodini, G. et al. Correlation between tectonic CO₂ Earth degassing and seismicity is revealed by a 10-year record in the Apennines, Italy. *Sci. Adv.* **6**, eabc2938 (2020).
83. Frezzotti, M. L., Peccerillo, A. & Panza, G. Carbonate metasomatism and CO₂ lithosphere-asthenosphere degassing beneath the Western Mediterranean: An integrated model arising from petrological and geophysical data. *Chem. Geol.* **262**, 108–120 (2009).

84. Girault, F. & Perrier, F. The Syabru-Bensi hydrothermal system in central Nepal: 2. modeling and significance of the radon signature. *J. Geophys. Res. Solid Earth* **119**, 4056–4089 (2014).
85. Girault, F. et al. Large-scale organization of carbon dioxide discharge in the Nepal Himalayas. *Geophys. Res. Lett.* **41**, 6358–6366 (2014).
86. Miller, S. A. et al. Aftershocks driven by a high-pressure CO₂ source at depth. *Nature* **427**, 724–727 (2004).
87. Sibson, R. H. Earthquake rupturing in fluid-overpressured crust: how common? *Pure Appl. Geophys.* **171**, 2867–2885 (2014).
88. Girault, F. et al. Persistent CO₂ emissions and hydrothermal unrest following the 2015 earthquake in Nepal. *Nat. Comm.* **9**, 2956 (2018).
89. Newton, R. C. & Manning, C. E. Role of saline fluids in deep-crustal and upper-mantle metasomatism: insights from experimental studies. *Geofluids* **10**, 58–72 (2010).
90. Halls, C. & Zhao, R. Listvenite and related rocks: perspectives on terminology and mineralogy with reference to an occurrence at Cregganbaun, Co., Mayo, Republic of Ireland. *Mineral Deposita* **30**, 303–313 (1995).
91. Johannes, W. An experimental investigation of the system MgO-SiO₂-H₂O-CO₂. *Am. J. Sci.* **267**, 1083–1104 (1969).
92. Falk, E. S. & Kelemen, P. B. Geochemistry and petrology of listvenite in the Semail ophiolite, Sultanate of Oman: complete carbonation of peridotite during ophiolite emplacement. *Geochim. Cosmochim. Acta* **160**, 70–90 (2015).
93. Beinlich, A., Plümpner, O., Hövelmann, J., Austrheim, H. & Jamtveit, B. Massive serpentinite carbonation at Linnajavri, N-Norway. *Terra Nova* **24**, 446–455 (2012).
94. Menzel, M. D. et al. Carbonation of mantle peridotite by CO₂-rich fluids: formation of listvenites in the Advacate ophiolite complex Newfoundland, Canada. *Lithos* **323**, 238–261 (2018).
95. Schreyer, W., Ohnmacht, W. & Mannchen, J. Carbonate-orthopyroxenites (sagvandites) from Troms, Northern Norway. *Lithos* **5**, 345–364 (1972).
96. Ohnmacht, W. Petrogenesis of carbonate-orthopyroxenites (sagvandites) and related rocks from Troms, Northern Norway. *J. Petrol.* **15**, 303–324 (1974).
97. Bucher, K. & Stober, I. Interaction of mantle rocks with crustal fluids: sagvandites of the Scandinavian caledonides. *J. Earth Sci.* **30**, 1084–1094 (2019).
98. Huizenga, J. M. & Touret, J. Granulites, CO₂ and graphite. *Gondw. Res.* **22**, 799–809 (2012).
99. Evans, M. J., Derry, L. A. & France-Lanord, C. Geothermal fluxes of alkalinity in the Narayani river system of central Nepal. *Geoch. Geophys. Geos.* **5**, Q08011 (2004).
100. Evans, M. J., Derry, L. A. & France-Lanord, C. Degassing of metamorphic carbon dioxide from the Nepal Himalaya. *Geoch. Geophys. Geos.* **9**, Q04021 (2008).
101. Lemonnier, C. et al. Electrical structure of the Himalaya of Central Nepal: High conductivity around the mid-crustal ramp along the M.H.T. *Geophys. Res. Lett.* **26**, 3261–3264 (1999).
102. Cattin, R. & Avouac, J. P. Modeling mountain building and the seismic cycle in the Himalaya of Nepal. *J. Geophys. Res. Solid Earth* **105**, 13389–13407 (2000). B6.
103. Bollinger, L., Avouac, J. P., Cattin, R. & Pandey, M. R. Stress buildup in the Himalaya. *J. Geophys. Res.* **109**, B11405 (2004).
104. Avouac, J.-P. Mountain Building: From Earthquakes to Geologic Deformation. In *Treatise on Geophysics* (ed. Schubert, G.) 2nd edition, Vol. 6, 381–432 (Elsevier, 2015).
105. Wannamaker, P. E., Caldwell, T. G., Doerner, W. M. & Jiracek, G. R. Fault zone fluids and seismicity in compressional and extensional environments inferred from electrical conductivity: the New Zealand Southern Alps and US Great Basin. *Earth, Planets and Space* **56**, 1171–1176 (2004).
106. Nesbit, B. E. Electrical resistivities of crustal fluids. *J. Geophys. Res.* **98**, 4301–4310 (1993).
107. Godard, G. Two orogenic cycles in eclogite-facies gneisses of the Southern Armorican Massif (France). *Eur. J. Mineral.* **21**, 1173–1190 (2009).
108. Hofer, G., Wagreich, M. & Neuhuber, S. Geochemistry of fine grained sediments of the upper Cretaceous to Paleogene Gosau Group (Austria, Slovakia): Implications for paleoenvironmental and provenance studies. *Geosci. Front.* **4**, 449–468 (2013).
109. McLennan, S. M., Hemming, S., McDaniel, D. K. & Hanson, G. N. Geochemical approaches to sedimentation, provenance, and tectonics. *GSA Special Paper* **284**, 21–40 (1993).
110. Connolly, J. A. D. Multivariable phase diagrams: an algorithm based on generalized thermodynamics. *Am. J. Sci.* **290**, 666–718 (1990).
111. Connolly, J. A. D. The geodynamic equation of state: what and how. *Geoch. Geophys. Geos.* **10**, Q10014 (2009).
112. Holland, T. J. B. & Powell, R. An internally consistent thermodynamic data set for phases of petrologic interest. *J. Metam. Geol.* **16**, 309–343 (1998).
113. Massonne, H. J. Phase relations and dehydration behaviour of calcareous sediments at very-low to low grade metamorphic conditions. *Period. Mineral.* **79**, 21–43 (2010).
114. Kuhn, B. K., Reusser, E., Powell, R. & Günther, D. Metamorphic evolution of calc-schists in the Central Alps, Switzerland. *Schweiz. Mineral. Petrogr. Mitt.* **85**, 175–190 (2005).
115. Holland, T., Baker, J. & Powell, R. Mixing properties and activity-composition relationships of chlorites in the system MgO-FeO-Al₂O₃-SiO₂-H₂O. *Eur. J. Mineral.* **10**, 395–406 (1998).
116. Coggon, R. & Holland, T. J. B. Mixing properties of phengitic micas and revised garnet-phengite thermobarometers. *J. Metam. Geol.* **20**, 683–696 (2002).
117. Auzanneau, E., Schmidt, M. W., Vielzeuf, D. & Connolly, J. A. D. Titanium in phengite: a geobarometer for high temperature eclogites. *Contrib. Mineral. Petrol.* **159**, 1–24 (2010).
118. White, R. W., Powell, R. & Holland, T. J. B. Progress relating to calculation of partial melting equilibria for metapelites. *J. Metam. Geol.* **25**, 511–527 (2007).
119. Newton, R. C., Charlu, T. V. & Klepea, O. J. Thermochemistry of the high structural state plagioclases. *Geochim. Cosmochim. Acta* **44**, 933–941 (1980).
120. Thompson, J. B. & Hovis, G. L. Entropy of mixing in sanidine. *Am. Mineral.* **64**, 57–65 (1979).
121. Elmer, F. L., White, R. W. & Powell, R. Devolatilization of metabasic rocks during greenschist–amphibolite facies metamorphism. *J. Metam. Geol.* **24**, 497–513 (2006).
122. Rapa, G., Groppo, C., Mosca, P. & Rolfo, F. Petrological constraints on the tectonic setting of the Kathmandu Nappe in the Langtang-Gosainkund-Helambu regions, Central Nepal Himalaya. *J. Metam. Geol.* **34**, 999–1023 (2016).

Acknowledgements

This study was funded by the Italian Ministry of University and Research (PRIN 2017, Project no. 2017LMNLAW). M.L.F. acknowledges funding by MUR project Dipartimenti di Eccellenza 2018–2022.

Author contributions

All authors jointly conceived the study. C.G. performed the thermodynamic modeling and interpreted the results. M.L.F. interpreted the consequence of fluid immiscibility in terms of transport dynamics. F.R. and C.G. extended the results to the Himalayan orogeny and put them in a broader perspective. All authors discussed the results and their implications and participated in writing the paper.

Competing interests

The authors declare no competing interests. Maria Luce Frezzotti is an Editorial Board Member for *Communications Earth & Environment*, but was neither involved in the editorial review of nor the decision to publish this article.

Additional information

Supplementary information The online version contains supplementary material available at <https://doi.org/10.1038/s43247-022-00340-w>.

Correspondence and requests for materials should be addressed to Chiara Groppo.

Peer review information *Communications Earth & Environment* thanks Manuel Menzel and the other, anonymous, reviewer(s) for their contribution to the peer review of this work. Primary Handling Editors: Joe Aslin, Heike Langenberg. Peer reviewer reports are available.

Reprints and permission information is available at <http://www.nature.com/reprints>

Publisher's note Springer Nature remains neutral with regard to jurisdictional claims in published maps and institutional affiliations.



Open Access This article is licensed under a Creative Commons Attribution 4.0 International License, which permits use, sharing, adaptation, distribution and reproduction in any medium or format, as long as you give appropriate credit to the original author(s) and the source, provide a link to the Creative Commons license, and indicate if changes were made. The images or other third party material in this article are included in the article's Creative Commons license, unless indicated otherwise in a credit line to the material. If material is not included in the article's Creative Commons license and your intended use is not permitted by statutory regulation or exceeds the permitted use, you will need to obtain permission directly from the copyright holder. To view a copy of this license, visit <http://creativecommons.org/licenses/by/4.0/>.

© The Author(s) 2022